JOURNAL OF MATERIALS SCIENCE **40** (2005) 4873–4879

The effect of Al-substitution on structure and electrical properties of Mn-Ni-Zn ferrites

A. A. SATTAR, H. M. EL-SAYED
Physics Department, Faculty of Science, Ain Shams University, Cairo, Egypt
M. M. EL-TABEY
Physics and Mathematical Engineering Department, Faculty of Engineering, Menoufia University, Shebin El-Kom, Egypt

X-ray diffraction, Infra-red spectroscopy and scanning electron microscopy have been used to investigate the $Mn_{0.5}Ni_{0.1}Zn_{0.4}Al_xFe_{2-x}O_4$ system ($0 \leq x \leq 0.15$ in steps of 0.025). The analysis of IR spectra indicates the distribution of Al-ions between both A and B-sites. The electrical resistivity and thermoelectric power as a function of temperature and Al-content have been investigated. It is observed that the resistivity increases with increasing the Al-content. It is also found that the temperature variation of resistivity exhibits two breaks, each break is associated with a change in the activation energy. Measurement of the thermoelectric power reveals *n*-type conduction for all samples. The activation energies of all samples in the paramagnetic region are found to be greater than those in the ferrimagnetic region. The results are explained on the basis of the formation of spin polarons in the paramagnetic region.

1. Introduction

Mn-Zn and Ni-Zn ferrites are the most important ferrites from the applications point of view, where they are used in devices such as inductor cores, converters, magnetic heads, electromagnetic wave absorbers etc. Mn-Zn ferrites possess high initial permeability and large magnetization, but are not suitable for magnetic applications at high frequency due to their high electrical conductivity and therefore high power losses. Ni-Zn ferrites have high resistivity, low-dielectric loss and high Curie temperature but have relatively low initial permeability at high frequencies. Recently many authors have studied the combination of these two ferrites in order to obtain ferrites with favorable magnetic properties with low losses especially at high frequencies. The microstructure, magnetic properties and dc resistivity of $Mn_xNi_{0.5-x}Zn_{0.5}Fe_2O_4$ ferrites, prepared using a citrate precursor method has been investigated [1, 2]. Unfortunately, the resistivity decreased with increasing Mn-content. The effect of sintering and microstructure on the initial permeability for $Ni_{0.68}Mn_{0.02}Zn_{0.25}Fe_{2.05}O_4$ and $Mn_{0.2}Ni_{0.2}Zn_{0.6}Fe_2O_4$ were studied [3, 4]. It was found that, the sintering temperature has a great effect on the structural and magnetic properties of these ferrites. Finally, the Mn-substitution effect on the conductivity, magnetic properties and dielectric behavior of Ni-Zn ferrites was carried out [5, 6]. They found that, in spite of there was an enhancement in the saturation magnetization, the initial permeability, Curie temperature and dc resistivity were decreased with increasing Mn-content. In the present work, the effect of Al-substitution on the IR spectra, the micro structural and the electrical properties of $Mn_{0.5}Ni_{0.1}Zn_{0.4}Al_xFe_{2-x}O_4$ ferrites will be studied.

2. Experimental procedure

Ferrite samples with chemical formula $Mn_{0.5}Ni_{0.1}Zn_{0.4}Al_xFe_{2-x}O_4$ ($x = 0$ to $x = 0.15$, with step 0.025) were prepared by a conventional ceramic method. High purity oxides, 99.99%, of NiO, ZnO, Al_2O_3 and Fe_2O_3 with $MnCO_3$ were mixed together according to their molecular weights. The mixture of each composition was ground to a very fine powder and presintered at 900°C for 15 h. The presintered mixture was ground again and pressed at room temperature under a pressure of 3.8×10^8 Pa into tablet form. They were finally sintered at 1300°C for 4 h in two cycles and then slowly cooled in N_2 atmosphere to room temperature at a rate of 1°C /min.

X-ray diffraction patterns were performed using a diffractometer type X'Pert Graphics & Identify with Cu K_α radiation. The density d of each composition was measured in toluene using Archimedes principle. The porosity percentage (P%) was calculated according to the relation $P = 100\ [1 - (d/d_x)]\%$ where d_x is the X-ray density. The FTIR spectra were carried out (using 1650 Perkin Elmer spectro-photometer) in the range from 200–600 cm^{-1}. The grain size was obtained by low vacuum Scanning Electron Microscope (type JEOL JSM5600). The dc resistivity of the samples was measured using the two-probe method with In-Hg contacts. Thermoelectric power measurements were carried out by the differential method. The sample holder for measuring thermo-e.m.f. consisted of

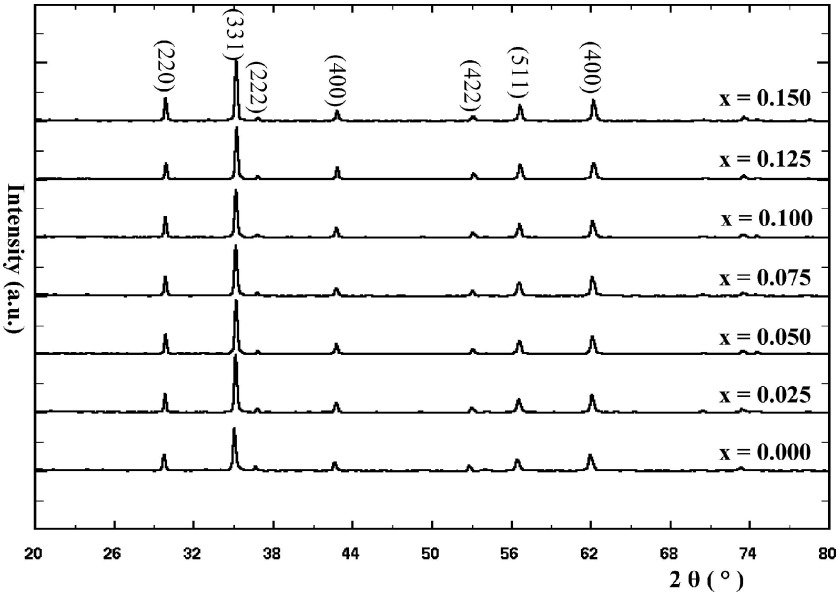

Figure 1 X-ray batterns of the investigated samples.

two non-magnetic copper electrodes between which the sample was firmly fixed. An auxiliary heater was fixed to the lower electrode for additional heating in order to maintain a temperature gradient of about 12 K/cm for all investigated samples. Themo-e.m.f. was measured using a 4-bit digital mutimeter (model Keithley 175). The temperature was measured using a chromel—alumel thermocouple.

3. Results and discussion

3.1. X-Ray measurements

The formation of single phase $Mn_{0.5}Ni_{0.1}Zn_{0.4}Al_xFe_{2-x}O_4$ ferrite was confirmed by the XRD patterns of the investigated samples as shown in Fig. 1. The values of lattice parameters and porosity (P%) are plotted as a function of Al-ion concentration in Fig. 2. It is clear that as the Al-concentration increases, the lattice parameter decreases while the porosity increases. Similar behavior was observed in Al-substituted Mn-Zn [7, 9] and Ni-Zn ferrites [10]. The decrease in lattice parameter with Al-concentration can easily be explained on the basis of the ionic radii where, the radius

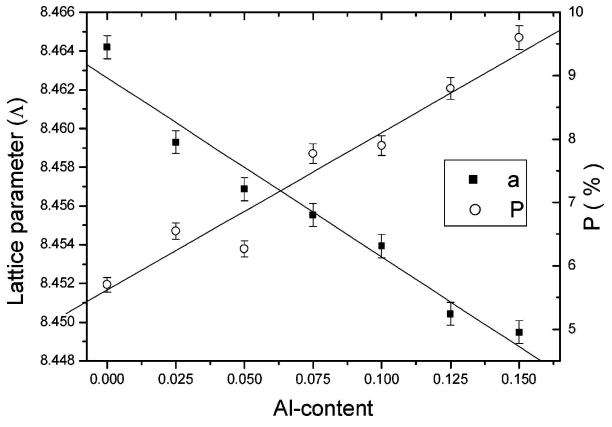

Figure 2 The variation of the lattice constant a (Å) and porosity P(%) with Al-Content.

of Al-ion (≈0.51 Å) is smaller than that of the iron ion (≈0.67 Å).

For the spinel structure, the theoretical lattice parameters a_{th} could be calculated using the following equation [11]

$$a_{th} = \frac{8}{3\sqrt{3}}[(r_A + r_O) + \sqrt{3}(r_B + r_O) \qquad (1)$$

where r_o is the radius of the oxygen ion (1.32 Å), r_A and r_B are the ionic radii of tetrahedral (A-site) and octahedral (B-site) sites, respectively. To calculate r_A and r_B, the following cation distribution is assumed;

$$\left(Al_t^{3+}Zn_{0.4}^{2+}Fe_{0.2}^{3+}Mn_{0.4-t}^{2+}\right)\left[Al_{x-t}^{3+}Mn_{0.1+t}^{2+}Ni_{0.1}^{2+} \times Fe_{1.8-x-y}^{3+}Fe_y^{2+}\right]O_4$$

This cation distribution is based on the following:

(I) For the unsubstituted sample, 80% of Mn-ions occupy the tetrahedral position (A-site) and the remaining, 20%, occupy the octahedral position (B-site) [12]. While, for the substituted samples, this ratio is slightly changed due to Al-substitution.

(II) It is well known that, Zn^{2+} ions prefer to occupy the tetrahedral sites while Ni $^{2+}$ ions occupy the octahedral sites.

(III) Concerning Al^{3+}-ion distribution, there are two points of view. The first one is that, Al^{3+}-ions in spinel ferrites are distributed on both tetrahedral and octahedral sites, such that, the majority of Al-ions occupy the octahedral position (B-site) [13–19]. The other one is that the substituted Al^{3+}- ions completely occupy B-sites [10, 20–22]. IR spectroscopic analysis, as will be discussed later, shows that Al^{3+} ions are distributed in both A and B-sites.

In this cation distribution, the formation of Fe^{2+}-ion during the sintering process is taken into consideration.

TABLE I The values of t and y with Al-concentration

Al-Conc. (x)	(t)	Fe^{2+}-Conc.(y)
0.000	0	0.18
0.025	0.012	0.17
0.050	0.020	0.162
0.075	0.024	0.155
0.100	0.030	0.146
0.125	0.037	0.126
0.150	0.040	0.114

The ionic radius for each site is calculated according to the following equations

$$r_A = (t r_{Al^{3+}} + 0.4 r_{Zn^{2+}} + 0.2 r_{Fe^{3+}} + (0.4 - t) r_{Mn^{2+}})$$

$$r_B = \frac{1}{2}[(x - t) r_{Al^{3+}} + (0.1 + t) r_{Mn^{2+}} + 0.1 r_{Ni^{2+}} + (1.8 - x - y) r_{Fe^{3+}} + y r_{Fe^{2+}}]$$

where $r_{AL^{3+}}$, $r_{Zn^{2+}}$, $r_{Mn^{2+}}$, $r_{Fe^{3+}}$ and $r_{Ni^{2+}}$ are the ionic radii of aluminum, zinc, manganese, iron and nickel respectively. The values of the ionic radii are taken from [23] where the ionic radius depends on the coordination number. The values of t and y in the assumed cation distribution, which are listed in Table I, were chosen as fitting parameters such that good fitting between a_{Th} and a_{Exp} is obtained.

3.2. Porosity and grain size

From Fig. 2 one notes that, as Al-content increases the porosity ($P\%$) increases. It is known that, the porosity of ceramic samples results from two sources, intragranular porosity (P_{intra}) and intergranular porosity (P_{inter}) [24]. Thus the total porosity ($P\%$) could be written as the sum of the two types i.e.,

$$P(\%) = (P_{intra} + P_{inter}) \quad (2)$$

Furthermore, it was reported that the intergranular porosity (P_{inter}) depends on the grain size [8, 24]. By studying the SEM for the samples, it is found that as the Al-concentration increase from $x = 0.05$ up to $x = 0.15$ there is no considerable change in the grain size Fig. 3. Therefore as Al-content increases the intergranular porosity (P_{inter}) remains almost constant. Thus according to Equation 2, the increase of the total porosity $P(\%)$ results mainly from the increase of intragranular porosity (P_{intra}) with Al-concentration. Such a conclusion is in agreement with that previously reported [9, 20].

3.3. IR-spectral analysis

The study of Far-infra-red spectroscopy is an important tool in obtaining information regarding the positions of the ions in the crystal through the crystal's vibrational modes [25]. It is known that the normal and inverse cubic spinels have four IR bands representing the four fundamentals {ν_1, ν_2, ν_3 and ν_4} [26]. It has been reported that, the first three IR fundamental bands are due to tetrahedral and octahedral complexes, while the fourth one is due to the lattice vibrations [25]. Fig. 4 shows the IR spectra of some studied samples ($x = 0.0$, 0.05, 0.1 and 0.15). The positions of their bands are given in

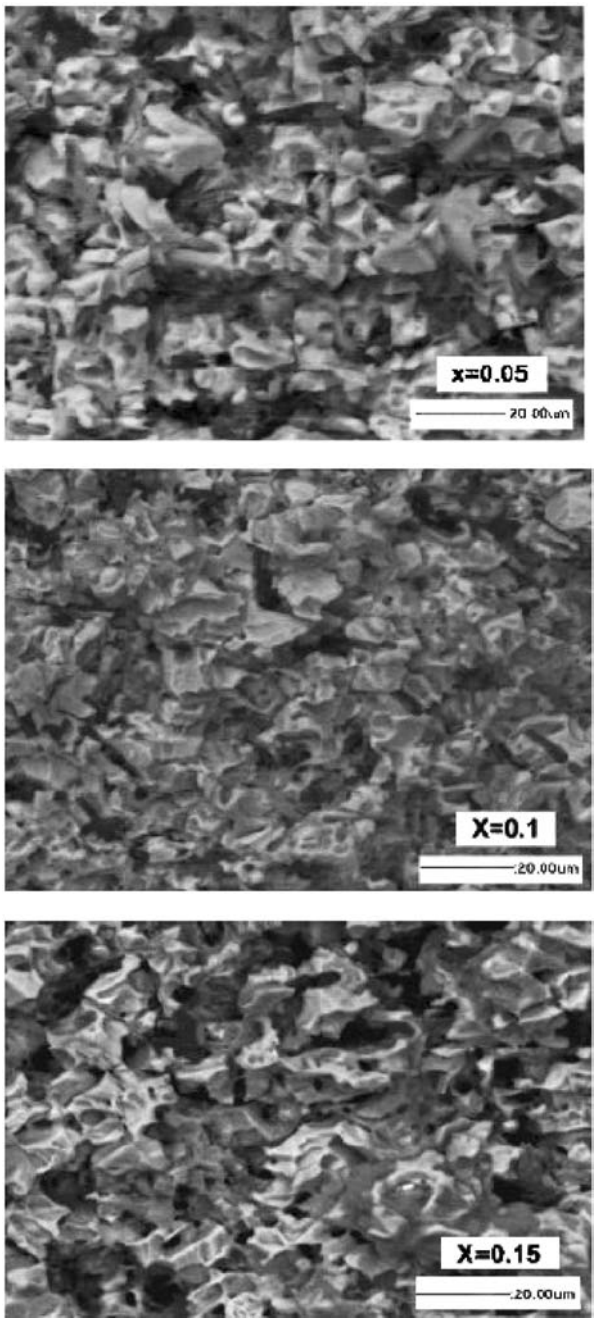

Figure 3 SEM micrographs of the samples of x = 0.05, 0.10 and 0.15.

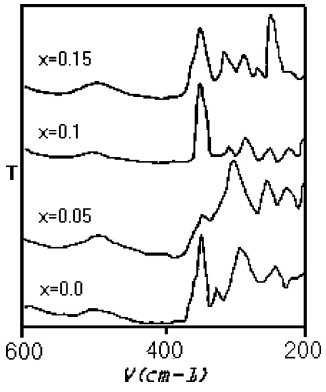

Figure 4 IR-spectrum of samples with x = 0.0, 0.05, 0.10 and 0.15.

TABLE II Frequency (cm^{-1}) of the IR observed bands

Al-Conc. (x)	Tetra.	Octahedral bands			Lattice vibration		
	ν_1	ν_2	ν_3		ν_4		
0.00	547	409	344	324	272	240	222
0.05	553	398	348	319	277	249	221
0.10	559	397	343	307	278	248	220
0.15	561	378	344	310	288	240	222

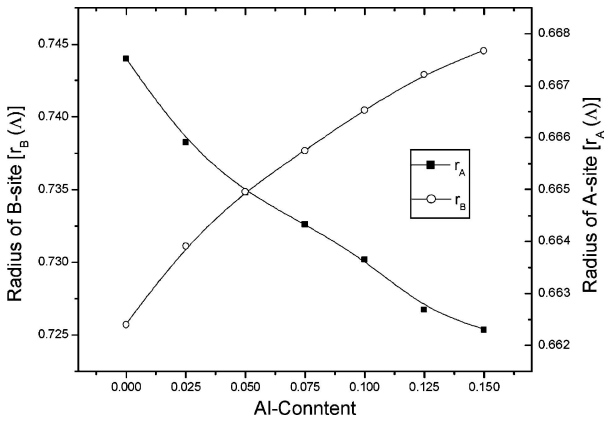

Figure 5 Variation of tetra. and octahedral redii with Al-content.

Table II. The high frequency bands ν_1 (547–561) and ν_2 (378–409) are attributed to the vibration of iron ions in tetrahedral and octahedral positions respectively. The third vibrational frequency band ν_3 (310–344) is associated with the divalent octahedral metal ions and oxygen complexes. Finally, the fourth vibrational band (ν_4) (220–288) is attributed to the lattice vibrational frequency [27].

It is obvious from the table that as the Al-concentration (x) increases ν_1 shifts to higher frequency while ν_2 shifts to lower frequency. These shifts in the frequencies of the bands could be explained on the basis that, the change in the bond length has an inverse relation with the band frequency shift [7]. Fig. 5 shows the variation of the radius of tetrahedral site (r_A) and octahedral site (r_B) with Al-content. It is clear that as Al-concentration increases, $r_A$decreases while r_B increases, which explain the increase of ν_1 and the decrease of ν_2 and ν_3. The shift of the lattice vibration band ν_4 to higher frequency could be attributed to the difference in masses between the substituted and displaced ions. In our composition, Fe^{3+}-ions are replaced by Al^{3+}-ions, which have smaller mass than that of Fe^{3+}. Thus, total mass of lattice decreases leading to an increase of the frequency band ν_4.

3.4. DC electrical resistivity

The temperature dependence of the electrical resistivity of the sample with $x = 0.05$ is shown in Fig. 6, as an example. It is clear that, $\log(\rho)$ has a linear relation with the inverse of temperature ($1000/T$). This behavior could be described according to the relation

$$\rho = \rho_o \, \mathrm{Exp} - (E/KT)$$

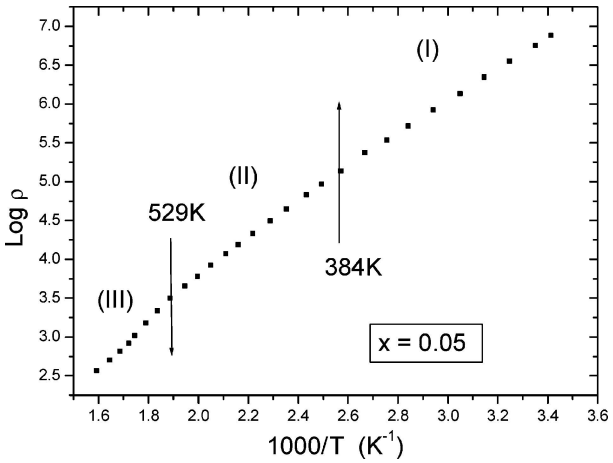

Figure 6 Variation of resistivity (Log ρ) with inverse temperature ($1000/T$).

where E is the activation energy, K is Boltzmann constant, ρ_o is a temperature independent constant.

The variation of resistivity with temperature for all investigated samples could be divided into three linear regions with different activation energies. Similar behavior was reported for Ni-Zn ferrites [28–30] and Ni-Cd ferrites [31–33]. The first region ranged from room temperature up to 380 K, for all investigated samples. The conduction phenomena in this region is attributed to an extrinsic conduction mechanism (impurities) [28–33].

By comparing the values of transition temperatures between the second and third regions $(T_C)_{elect.}$, with Curie temperatures determined from magnetic measurements $(T_C)_{mag.}$ (Table III), one notes that the two sets of values are close to each other. Therefore, the change in activation energies between regions II and III is attributed to the magnetic transition from order to disorder state.

The variation of activation energies in the second, E_{ferri}, and third regions, E_{para}, with Al- concentration is shown in Fig. 7. It is observed that (E_{para}) is greater than (E_{ferri}) for all investigated samples. The increase of the activation energy from ordered to disorder state was attributed to the volume expansion above T_c, which is accompanied by an endothermic peak in DSC (Differential Scanning Calorimetry) [34]. However, in the investigated samples, DSC indicated the presence of good thermal stability as shown in Fig. 8. Therefor, the absence of the DSC endotherm associated with volume expansion in the present study suggests that the

TABLE III Variation of activation energies and Curie temperatures with Al-concentration

Al-conc. (x)	E_ρ (eV) 2nd region	E_μ (eV) 2 nd region	$(T_C)_{elect.}$ (K)	$(T_C)_{mag.}$ (K)
0	0.95	0.95	435	431
0.025	1.02	0.96	519	513
0.05	1.02	0.95	529	528
0.075	1.01	0.97	509	507
0.1	1.02	0.97	508	495
0.125	1.04	1.01	503	508
0.15	1.03	1.01	495	500

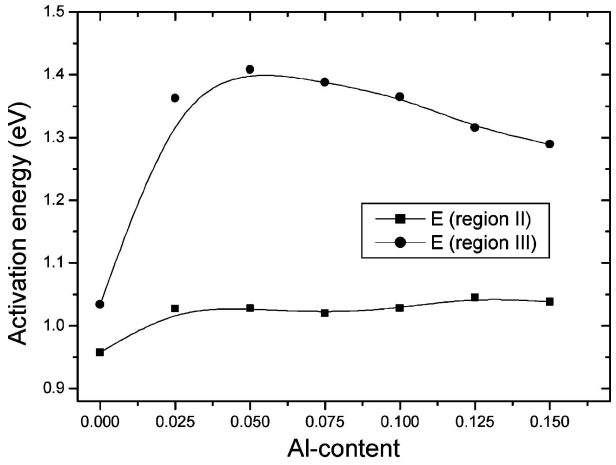

Figure 7 Change of activation energies with Al-content.

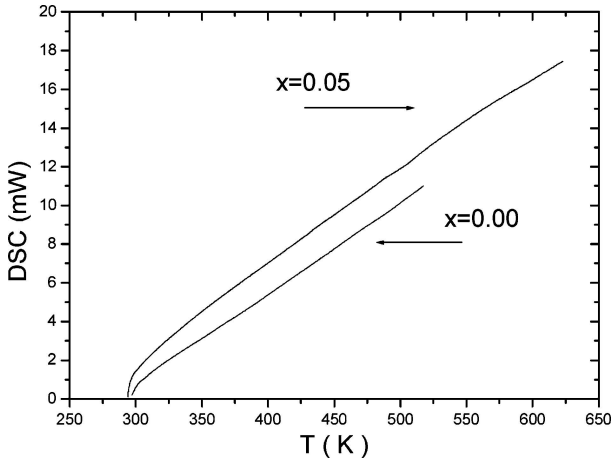

Figure 8 The temperature dependence of DSC.

observed change in activation energy is unlikely to be accounted for by this phenomenon.

The spin polaron model could be used to explain the increase of activation energy. According to this model the total energy of the spin polaron is given by [35];

$$E = \frac{5\hbar^2\pi^2}{6m}\left(\frac{4mJ_2}{\hbar^2\pi a^3}\right)^{2/5} - J_1 \qquad (2)$$

where, m is the electron mass, a is the lattice constant, J_1 is the exchange energy between the spin of the conduction electron and ion spins and J_2 is the exchange energy between the ion spins. The spin polaron will be formed only if the value of E in Equation 2 is negative which means that the moments are fully oriented parallel to that of the conduction electrons. For $T < T_c$, the ionic magnetic moments are parallel (i.e. $J_2 > J_1$) and the magnetic spin polaron has a small effect. On the other hand, for $T > T_c$, the magnetic ionic moments are randomly oriented (i.e. $J_2 < J_1$) so the contribution of magnetic spin polaron becomes effective. Hence, the effective mass of the conduction electrons will increase due to the magnetic polarization between the conduction electrons and the magnetic ions, which causes the formation of spin polaron [36, 37]. This means that, the activation energy of spin polaron (E_s) should be added to that in the ferri magnetic region i.e. $E_{(\text{para})} = E_{(\text{Ferri})} + E_s$. Moreover, it was reported that the activation energy E_s is roughly proportional to the paramagnetic susceptibility (χ_{para}) since it depends on the extent to which the lattice spins can swing parallel to the spin of the conduction electron [38]. To check this relation, Fig. 8 shows the dependence of both the initial permeability (μ_i), which is roughly proportional to χ_{para}, and E_S ($E_S = \Delta E = E_{\text{para}} - E_{\text{Ferri}}$) on Al-concentration. It is clear that, both μ_i and ΔE have the same behavior, they increase with Al-content to reach a maximum at $x = 0.05$ and begin to decrease with increasing x, which supports the assumption of spin polaron-formation.

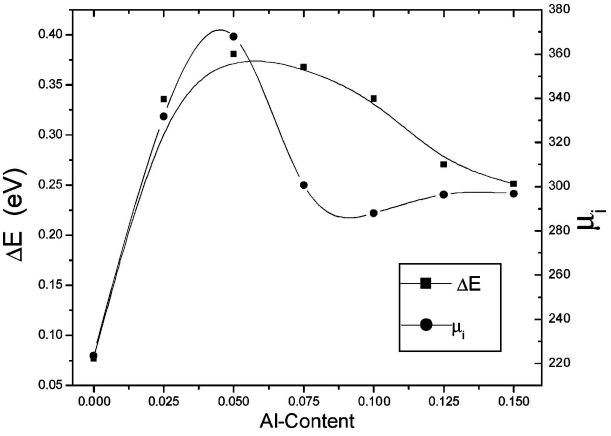

Figure 9 The change of $\Delta E(\%)$ and χ_{para} with Al-Content.

The dependence of electrical resistivity (ρ), at room temperature, and the concentration of Fe^{2+}-ion on the Al-content is shown in Fig. 10. It is clear that, the substitution of Al ion leads to increase the resistivity of all investigated samples. This behavior could be explained in terms of two factors:

(I) As the Al-concentration increases the concentration of Fe^{2+}-ions decreases and so the hopping probability between Fe^{3+} and Fe^{2+}-ions decreases which leads to increase the resistivity.

(II) The increase of Al-content leads to increase the intragranular porosity which in turn hinders the motion of charge carriers producing an increase of ρ.

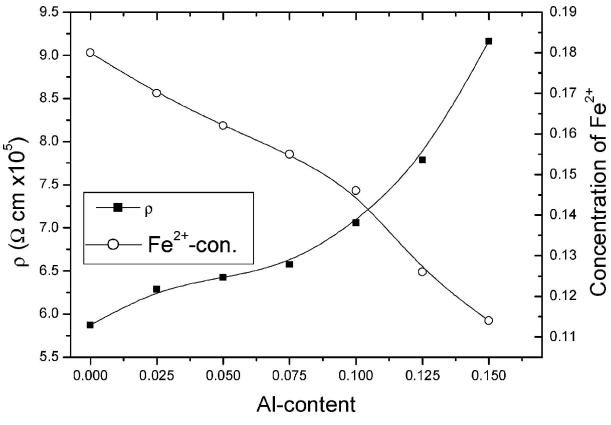

Figure 10 The variation of resistivity (ρ) and the concentration of Fe^{2+}-ion with Al-Content.

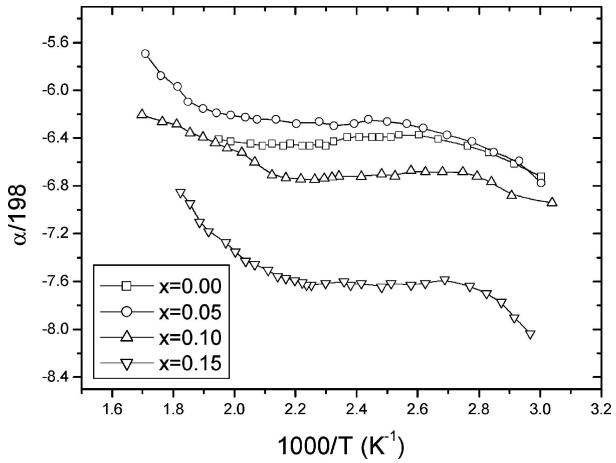

Figure 11 The temperature dependence of thermo-power of the samples with $x = 0.0$, 0.05, 0.10 and 0.15.

3.5. Thermoelectric power

Fig. 11 shows the change of $(\alpha/198)$ with inverse of temperature $(1000/T)$. It is obvious that, the sign of (α) for all investigated samples is negative which indicates that majority of charge carriers are electrons. The variation of $(\alpha/189)$ with temperature shows also three regions corresponding to those observed in $\rho(T)$ curves. The transition temperature of each region is nearly close to that obtained from the resistivity measurements.

To get more information about the conduction mechanism of these samples the charge carrier mobility (μ) is calculated using the values of ρ and α at different temperature by the following formulae [39]

$$\log \rho = \log(1/\mathrm{ne}\mu);$$

and

$$n = N_{\mathrm{o}}\mathrm{Exp}(-e\alpha/K)$$

where n is the charge carrier concentration, N_{o} is the density of states, which represents the concentration of Fe^{3+}-ions in the sample [40], and e is the electron charge.

Fig. 12 shows the dependence of log μ on the inverse temperature in the second region. It is clear that, the mobility increases strongly with increasing temperature. The activation energy calculated from the mobility (E_μ) is shown in Table III. It is obvious that, the values of E_μ are very close to those of E_{ferri}. This means that, the conductivity of the samples depends mainly on the charge carrier mobility rather than the charge carrier concentration. In addition, it is noted that the values of the activation energies, E_{ferri}, are greater than 0.5 eV for all the samples. These values are much higher than that for ionization of electrons or holes (i.e $E_{\mathrm{i}} \approx 0.1$ eV) and for Fe^{2+} to Fe^{3+} normal transition (i.e. $E \approx 0.2$ eV) which indicates that, the small polaron hopping mechanism is favored [8, 41].

4. Conclusions

The X-ray analysis illustrated the formation of single spinel phase while the IR-spectra indicated that Al^{3+} ions are distributed between tetrahedral and octahedral sites. The results of the electrical resistivity and thermoelectric power are consistent with the formation of spin polarons.

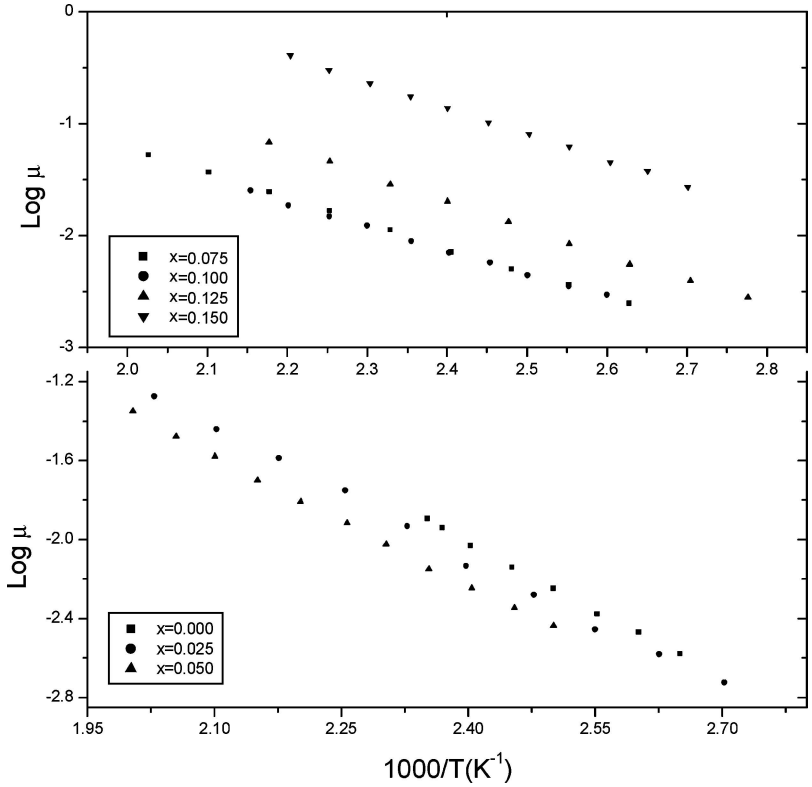

Figure 12 The dependence mobility (log μ) on the temperature $(1000/T)$.

References

1. AMARENDRA K. SINGH, T. C. GOEL and R. G. MENDIRATTA, *J. Appl. Phys.* **92**(7) (2002) 3872.
2. AMARENDRA K. SINGH, A. VERMA, O. P. THAKUR, CHANDRE PRAKASH, T. C. GOEL and R. G. MENDIRATTA, *Jpn. J. Appl. Phys.* **41** (2002) 5142.
3. JAPES BERA, ASHIM KUMAR SAMANTA and M. ARAVIND, in Procc. of (ICF 8), Kyoto and Tokyo, Japan (2000) p. 536.
4. AMARENDRA K. SINGH, T. C. GOEL and R. G. MENDIRATTA, *Phys. Stat. Sol.* (a) **201** (2004) 1453.
5. *Idem.*, *Jpn. J. Appl. Phys.* **42** (2003) 2690.
6. E. REZLESCU, L. SACHELARIE, P. D. POPA and N. REZLESCU, *IEEE Trans. Magn.* **36**(6) (2000) 3962.
7. G. CHANDRASEKARAN, S. SELVANDAN and K. MANIVANNANE, *J. Mat. Sci.: Mater. Electr.* **15** (2004) 15.
8. N. REZLESCU, E. REZLESCU, C. PASNICU and M. L. CRAUS, *J. Phys. Condens. Matter.* **6** (1994) 5707.
9. CHANDRA PRAKASH, *J. Mater. Sci. Lett.* **6** (1987) 651.
10. S. V. KAKATKAR, S. S. KAKATKAR, R. S. PATIL, P. K. MASKAR, A. M. SANKAPAL, S. S. SURYAWANSHI, N. D. CHAUDHARI and S. R. SAWANT, *J. Mag. Mag. Mat.* **159** (1996) 361.
11. S. A. MAZEN, M. H. ABDALLAH, B. A. SABRAH and H. A. M. HASHEM, *Phys. Stat. Sol.* (a) **134** (1992) 263.
12. F. PETIL and M. LENGLET, *Solid State Commun.* **86** (1993) 67.
13. A. M. ABOELATA, S. M. ATTIA and T. M. MEAZ, *J. Solid State. Sci.* **6** (2004) 61.
14. V. URVI, S. BIMAL and R. KULKARNI, *Physica B* **262** (1999) 5.
15. SEO WOOK, YOUNG LEE, KWANG PYO and SUNGTTO, *J. Korean Phys. Soc.* **34**(4) (1999) 378.
16. R. KULKARNI, S. BIMAL and G. BALDHA, *J. Mag. Mag. Mat.* **159** (1996) 375.
17. T. JUNG, D. PARK and S. KWON, *IEEE. Trans. On Magnet.* **31**(6) (1995) 3979.
18. ASHFAQ AHMED, *J. Mat. Sci.* **27** (1992) 4120.
19. M. ROSENBERG, P. DEPPE and H. JANSSEN, *J. Appl. Phys.* **57**(1) (1985) 3740.
20. S. S. SURYAWANSHI, V. DESHPAND and S. R. SAWANT, *J. Mat. Chem. Phys.* **59** (1999) 199.
21. A. M. SANKPAL, S. V. KAKATKAR and S. R. SAWANT, *J. Mat. Sci.: Mater. Electr.* **9** (1998) 173.
22. N. SPARVIERI and N. P. CATTARI, *J. Mater. Chem. Phys.* **25** (1990) 167.
23. R. D. SHANNON and C. T. PREWITT, *Acta Cryst.* **B26** (1970) 1046.
24. W. D. KIGERY, H. K. BOWEN and D. R. UHLMANN "Introduction of Ceramics" John Wiley & Sons New York, London, 1975) 458.
25. K. MOHAN and VENUDHAR, *J. Mat. Sci. Lett.* **18** (1999) 13.
26. RAVENDER, *J. Mater. Lett.* **40** (1999) 205.
27. M. A. AHMED, *J. Vibrat. Spectr.* **30** (2002) 69.
28. B. V. BHISE, S. D. LOTKE and S. A. PATIL, *Phys. Stat. Sol.* (a) **157** (1996) 411.
29. B. V. BHISE, M. G. PATIL, M. B. DONGARE, S. R. SAWANT and S. A. PATIL, *Indian J. Pure Appl. Phys.* **30** (1992) 385.
30. G. K. JOSHI, A. Y. KHOT and S. R. SAWANT, *J. Mat. Sci.* **22** (1987) 1694.
31. S. A. PATIL, M. G. PATIL, V. C. MAHAJAN, A. K. GHATAGE, S. LOTKE and R. N. PATIL, *Phse. Trans.* **56** (1996) 21.
32. M. G. PATIL, V. C. MAHAJAN and S. A. PATIL, *Phys. Stat. Sol.* (a) **144** (1994) 415.
33. *Idem.*, *Solid State Commun.* **91**(8) (1994) 667.
34. A. A. SATAR, A. H. WAFIK and H. M. EL-SAYED, in Procedings of (ICF 8), Koyoto and Tokyo, Japan (2000).
35. N. F. MOTT and E. A. DAVIS, "Electronic Processes in Non-Crystalline Materials" (Clarendon Press, Oxford, 1971) p. 175.
36. T. WOLFRAM and H. J. CALLAWAY, *Phys. Rev.* **127** (1962) 1605.
37. A. L. ZILICHIKHIS and Y. P. IRKHIN, *Sov. Phys. Solid State* **10** (1969) 1554.
38. S. METHAFESSEL and D. C. MATTIS, *Hand Buch der Physik* **127** (1968) 439.
39. P. V. REDDY, V. D. REDDY and D. RAVINDER, *Phys. Stat. Sol.* (a) **127** (1991) 439.
40. YONG-CHAE CHUNG and HAN-ILL YOO, *J. Mater. Res.* **16**(3) (2001) 774.
41. B. L. PATIL, S. R. SAWANT, S. A. PATIL and R. N. PATIL, *J. Mat. Sci.* **29** (1994) 175.

Received 4 September
and accepted 10 December 2004